A Preliminary Assessment of Step Effects on the BOLT Geometry in Mach 6 Flow

Carey F. Scott, Scott A. Berry, Francis A. Greene
NASA Langley Research Center, Hampton, VA, 23681, USA

Kevin Basore and Stefan Wernz
Raytheon, Tucson, AZ, 85756, USA

An infrared thermography measurement technique has been installed in the Langley Aerothermodynamic Laboratory. The system is calibrated for use with commercially available thermoplastics and ceramic materials, and to the surface temperature ranges when exposed to the facility hypersonic flow. Herein an uncertainty quantification is performed, revealing 5% surface temperature and 20% heat transfer uncertainty bands to two-sigma confidence. As a first application of the test measurement technique, an investigation was conducted to explore the correlation between the height of forward facing (FF) and rearward facing (RF) two-dimensional steps, free stream Reynolds number, and the onset of boundary layer transition from laminar to turbulent in Mach 6 flow on a 50% scale Boundary Layer Transition (BOLT) flight test vehicle geometry. Computational predictions were generated to identify potential x/L locations of transition onset for various flow conditions with a smooth outer mold line geometry and are compared to experimental results. The BOLT Step Test was conducted in the NASA Langley Aerothermodynamic Laboratory 20-inch Mach 6 wind tunnel at Reynolds numbers between 1.4 and 11.3 million conditions for various step heights. Data were collected using a developmental infrared thermography test technique and reduced to heat transfer for comparison with CFD solutions. This is a preliminary assessment of the developmental infrared thermography test technique used to acquire and reduce the experimental data. insight into the ongoing comparative analysis of the effects of FF and RF steps on boundary layer transition for the BOLT geometry in Mach 6 flow.

I. Nomenclature

A. Symbols and Units

c_0 = speed of light, ms^{-1}
c_1 = first radiation constant, $W\text{-}m^2$
c_2 = second radiation constant, $m^2\text{-}K$
H = Stagnation enthalpy,
h = Enthalpy based heat transfer film coefficient (lbm/ft2-s) $\left(\frac{\dot{q}}{H_{aw}-H_w}\right)$
$\boldsymbol{h}$ = Planck's constant, J-s
h_{ref} = reference heat transfer coefficient using Fay-Riddell equation for stagnation point heating
$\boldsymbol{k}$ = Boltzmann's constant, J/K
k_B = baseline step height reference, inch
k_m = step height, measured, inch
$\boldsymbol{L}$ = Radiance, $W/m^2\text{-}sr$
L = characteristic length, ft
P = Pressure, psia
Re_θ = Reynolds number based on momentum thickness
S = camera units of intensity, counts
T = temperature, R, K
x = streamwise distance, inch

y	=	spanwise distance from centerline, inch
y_{ref}	=	characteristic span dimension, inch
α	=	angle of attack, degrees
$\hat{\alpha}$	=	fist emissivity function coefficient
β	=	yaw angle, degrees
$\hat{\beta}$	=	second emissivity function coefficient
δ	=	boundary layer thickness, inch
θ	=	momentum thickness, inch
λ	=	wavelength, micrometers

B. Acronyms

2D	2-Dimensional
3D	3-Dimensional
AFOSR	Air Force Office Of Scientific Research
AFRL	Air Force Research Laboratory
APL	Applied Physics Laboratory
BAM6QT	Boeing/AFOSR Mach 6 Quiet Tunnel
BLT	Boundary Layer Transition (phenomenology)
BOLT	Boundary Layer Transition or Turbulence (model/geometry)
BST	BOLT Step Test
CFD	Computational Fluid Dynamics
DN	Digital Numbers (counts)
FF	Forward Facing
FLIR	Forward Looking Infrared
HIFiRE	Hypersonic International Flight Research Experimentation
HTP	Hypersonic Technologies Project
IHEAT	Imaging for Hypersonic Experimental Aeroheating Testing
IR	Infrared
IRT	Infrared Thermography
JHU	Johns Hopkins University
LAL	NASA Langley Aerothermodynamics Laboratory
LaRC	NASA Langley Research Center
LAURA	Langley Aerothermodynamic Upwind Relaxation Algorithm
LWIR	Long-Wave Infrared
MPI	Message Passing Interface
MWIR	Mid-Wave Infrared
NEDT	Noise Equivalent Temperature Difference
NIR	Near-Infrared
NIST	National Institute of Standards and Technology
OML	Outer Mold-Line
PEEK	Polyether-Ether-Ketone
psia	Pounds Per Square Inch Absolute
RF	Rearward Facing
STVD	Symmetric Total Variational Diminishing
ZnSe	Zinc Selenide

II. Introduction

An ongoing series of sounding rocket flight experiments have been underway for more than a decade, first starting with the HIFiRE flights and now the follow up BOLT I (**Bo**undary **L**ayer ***T****ransition*) and BOLT II (**Bo**undary **L**ayer ***T****urbulence*) flights. BOLT is sponsored by the Air Force Research Laboratory (AFRL) Air Force Office of Scientific Research (AFOSR) to study hypersonic boundary layer transition on increasingly complex configurations. While most of the HIFiRE flights were conducted on simple shapes, such as straight or elliptic cones, the BOLT vehicle was intended to represent a more realistic configuration (similar to a wave-rider concept) with concave surfaces and swept leading edges (see Figure 1). The expectation is that BOLT would stress the national capability to analyze the boundary layer breakdown process, with multiple instability modes interacting and ultimately leading to transition from laminar to turbulent. There are presently two BOLT or BOLT-derivative flights considered for this wind tunnel experiment: BOLT I, led by Johns Hopkins University Applied Physics Laboratory (JHU/APL) as the prime contractor, which launched during May 2021 out of Esrange in Sweden; and BOLT II, with Texas A&M and CUBRC as the lead group, which launched during March 2022 out of NASA Wallops Flight Center in Virginia [1, 2].

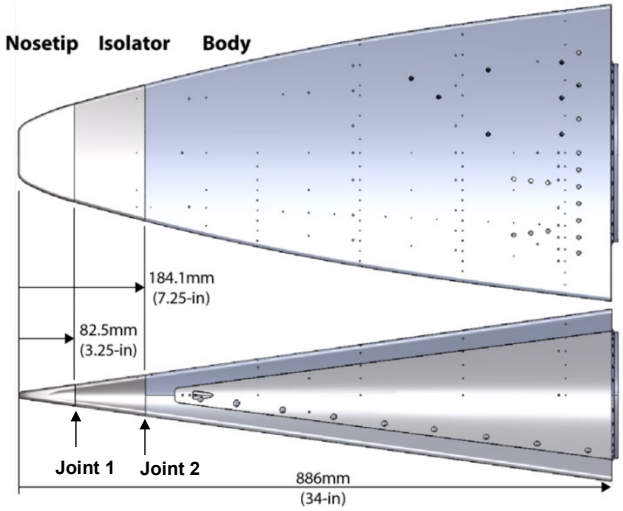

Figure 1. BOLT I Flight Vehicle Design**.**

During the final design phase of the BOLT I flight vehicle, a wind tunnel test entry was conducted in Purdue's Boeing/AFOSR Mach 6 Quiet Tunnel (BAM6QT) to investigate the effect of both forward facing (FF) and rearward facing (RF) steps [4]. Largely influenced by the uncertainty associated with 2D step effects on boundary layer transition in hypersonic flight, the decision was made to utilize RF steps on all joints and to size the steps such that the differential thermal growth of each part would result in RF steps throughout the flight test data collection windows (both ascent and descent). Ultimately, the BAM6QT study provided some guidance for the final decisions on the sensitivity of boundary layer transition due to 2D steps, but did not have the joint located in the same location as the flight configuration. The BOLT Step Test utilized a nose step location that accurately represents the step location on the BOLT I flight geometry.

The NASA Langley Research Center (LaRC) has been involved in the BOLT program from the beginning, providing the initial set of experimental aeroheating data for the project to anlayze [5]. More recently, and with the support of the Hypersonic Technologies Project (HTP), LaRC has initiated a series of wind tunnel studies to support various aspects of the research associated with the overall project [6]. The intent of the present experiment is to provide a controlled data set to assist in flight test data analyses, and serve to provide data for future design considerations. Other follow on testing by Berry et al. [3] focused on discrete 3D trips, rather than the 2D steps as was done here. The development of 2D steps at the joints between the nosetip and isolator (Joint 1), and between the isolator and body (Joint 2) is a result of the dicision to use different materials for for the nosetip, isolator and body on the flight vehicle.

The present study intends to provide details of one source of boundary layer tripping resulting from the incidence of the 2-dimensional step at the joint between the stainless-steel isolator and the aluminum body (Joint 2) caused by

differential rates of thermal expansion in the two materials on either side. Additional comparisons to other BOLT-derivtive geometries (Flat-BOLT) are presented in later sections for reference.

III. Boundary Layer Transition Measurements at LAL

Understanding the state of the boundary layer is crucial in hypersonic vehicle design problems. A laminar boundary layer provides lower skin friction but is more likely to separate. Conversely, a turbulent boundary layer increases skin friction, drag and surface heating due to enhanced vorticity and mixing but is less likely to separate. At hypersonic speeds, a turbulent boundary layer can cause heating rates several times higher than a laminar one which has significant impact to structural integrity. This increased heating can damage vehicles lacking proper thermal protection. Accurate assessment of boundary layer states is essential for extended high-speed systems and is an ongoing area of research for computational tool development and experimental methods for flight and ground testing.

Boundary layer transition from laminar to turbulent flow is thought to initiate with the entry of disturbances into the boundary layer. Depending on the model geometry and flow conditions, transition onset can be abrupt or gradual. Various factors, such as surface roughness (discrete or distributed) or acoustic noise in the freestream, can introduce disturbances into the flow. These disturbances induce instabilities in the boundary layer, which amplify and eventually breakdown to turbulence. Instabilities in the boundary layer have been extensively identified, classified, and studied at low and supersonic speeds. However, studying these instabilities at hypersonic speeds presents greater challenges due to the complex interactions between various second mode instabilities, thin shock layers, and presence of chemically reacting gases. The LaRC Aerothermodynamics Branch has an extensive history of using thermographic imagery to analyze boundary layer transition. One standard test methodology is the phosphor thermography technique developed and implemented at NASA LaRC over the last 30+ years. This methodology involves the acquisition of an image of the global surface temperature distribution on a model surfacewhich is used to interrogate the boundary layer state [7]. One limitation of the phosphor thermography test technique is the inability to spatially resolve small features on a model and their impact on heat transfer. The resolution of phosphor thermography at LAL is partly related to the roughness and uniformity of the phosphor coating which must be applied to models.

The experiment described herein focused on the development of an alternate data acquisition technique for Langley Aerodynamic Laboratories (LAL) using calibrated IR thermography and temperature-dependent heat transfer properties of a modern thermoplastic called polyether-ether-ketone, or PEEK. Modern infrared camera systems can provide significantly greater spatial resolution and thermal sensitivity when compared to the legacy phosphor thermography techniques and are well-suited for researching the effects of small surface features and discrete roughness elements on boundary layer transition in hypersonic flow.

IV. Experimental Methods

A. Test Facility & Conditions

The Langley 20-Inch Mach 6 Air Tunnel is a conventional blowdown tunnel in which heated, dried, and filtered air is used as the test gas. Freestream Reynolds numbers of 0.5×10^6/ft to 8×10^6/ft with stagnation temperatures of 805 °R to 935 °R can be produced for testing. The facility is equipped with a fast injection system that can place test models on the tunnel centerline in under 1 second. The test section is 20.5 x 20 in. and features large side windows for a schlieren imaging system and other optical test techniques. A key element of the 20-Inch Mach 6 Air Tunnel is the top-mounted IR-transmissive ZnSe window which was used in this experiment. Detailed information on LAL facilities can be found in [8].

A total of 78 runs were conducted to gather IR data for combinations of Reynolds numbers and step heights. Average flow parameters for the BOLT Step Test conditions are included in Table 1.

Table 1. 20-Inch Mach 6 Air Tunnel Conditions

Re_∞ (1/ft)	P_{t1} (psia)	T_{t1} (°R)	P_∞ (psia x 10^{-2})	T_∞ (°R)	V_∞ (ft/s)	M_∞
1.05	60	885	4.25	110.62	3039	5.89
2.03	125	910	8.12	111.66	3086	5.96
4.05	250	930	16.19	110.82	3092	6.01
5.69	365	935	23.11	112.98	3132	6.03
7.97	475	875	30.05	105.43	3012	6.02

B. BOLT Step Model

The BOLT Step Test (BST) model was designed such that the step height k at the Joint 2 position (see Figure 2) could be increased or decreased by known values to generate RF or FF steps. Increments of 0.005 inches were selected due to vendor concerns with stated limitations in repeatability of machined hardware. The design of an aluminum strongback to which the polyether-ether-ketone (PEEK) outer mold line would be fastened facilitated the fabrication of 21 separate stasinless steel adjustment blocks or 'inserts' to yield 41 possible model configurations via simple hardware changes. Each insert could be rotated by 180° to adjust the offset direction of the slot in the $\pm z$ direction to yield FF or RF step conditions. The test was designed to leverage previous BOLT test data [5,6] for numerous '0-step' cases, across various run conditions and develop an empirically derived transition model that incorporates Re_θ, step height, and boundary layer thickness. The aluminum strongback can also be used to conduct additional 2D step experiments by attaching different PEEK designs. One example of this is the Raytheon-sponsored 'Flat-BOLT' design, as shown in Figure 17, which was used to further explore the impact of the nose geometry on boundary layer transition. A Flat-BOLT design will enable the use of additional optical methods (focused schlieren or PLIF, for example) to probe the boundary layer. An optional extension of the BOLT I geometry and strongback support was

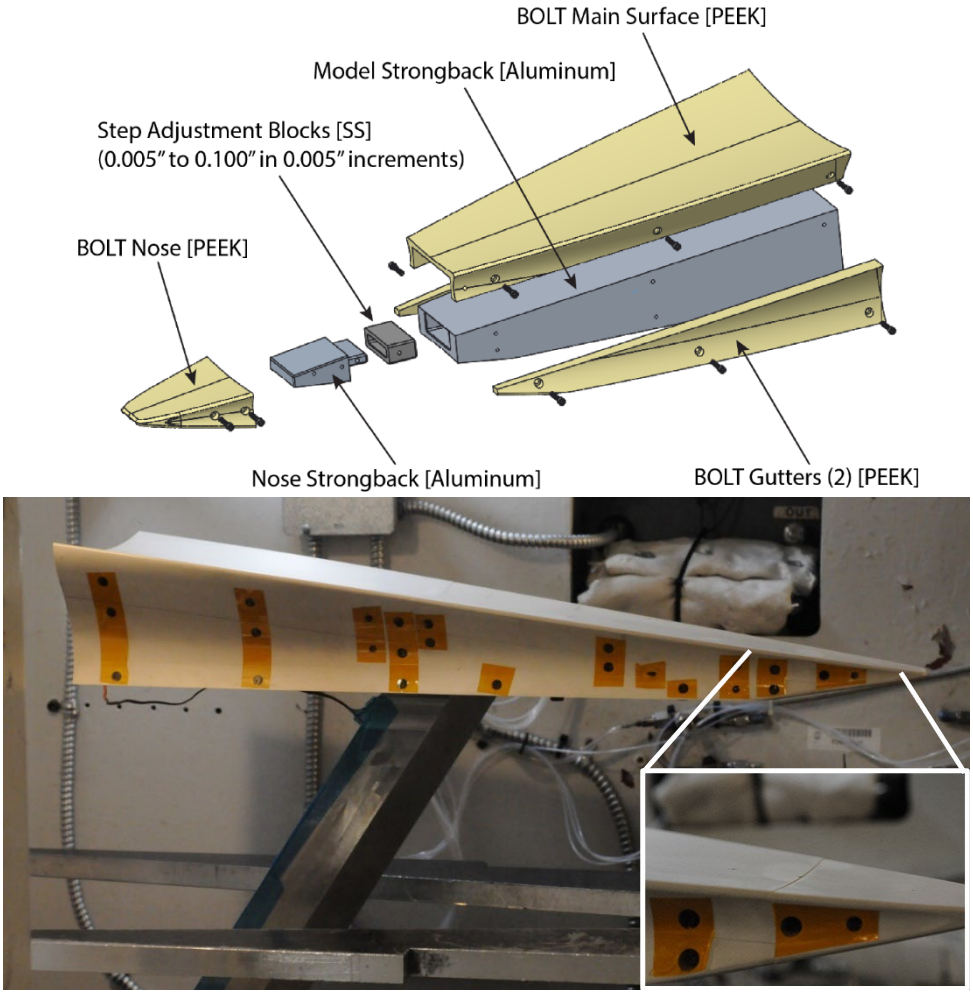

Figure 2. [Top] Exploded view of 50% scale BOLT Step Test model design and adjustable nose joint and aluminum strongbacks. [Bottom] Assembled BOLT Step Model with LONGBOLT extension which adds an additional length for future turbulence investigations.

developed for future studies of turbulent boundary layer phenomenology. The BST model with BOLT I + extension is referred to as the 'LONGBOLT' configuration and extends the BOLT I geometry by an additional 12.1 inches.

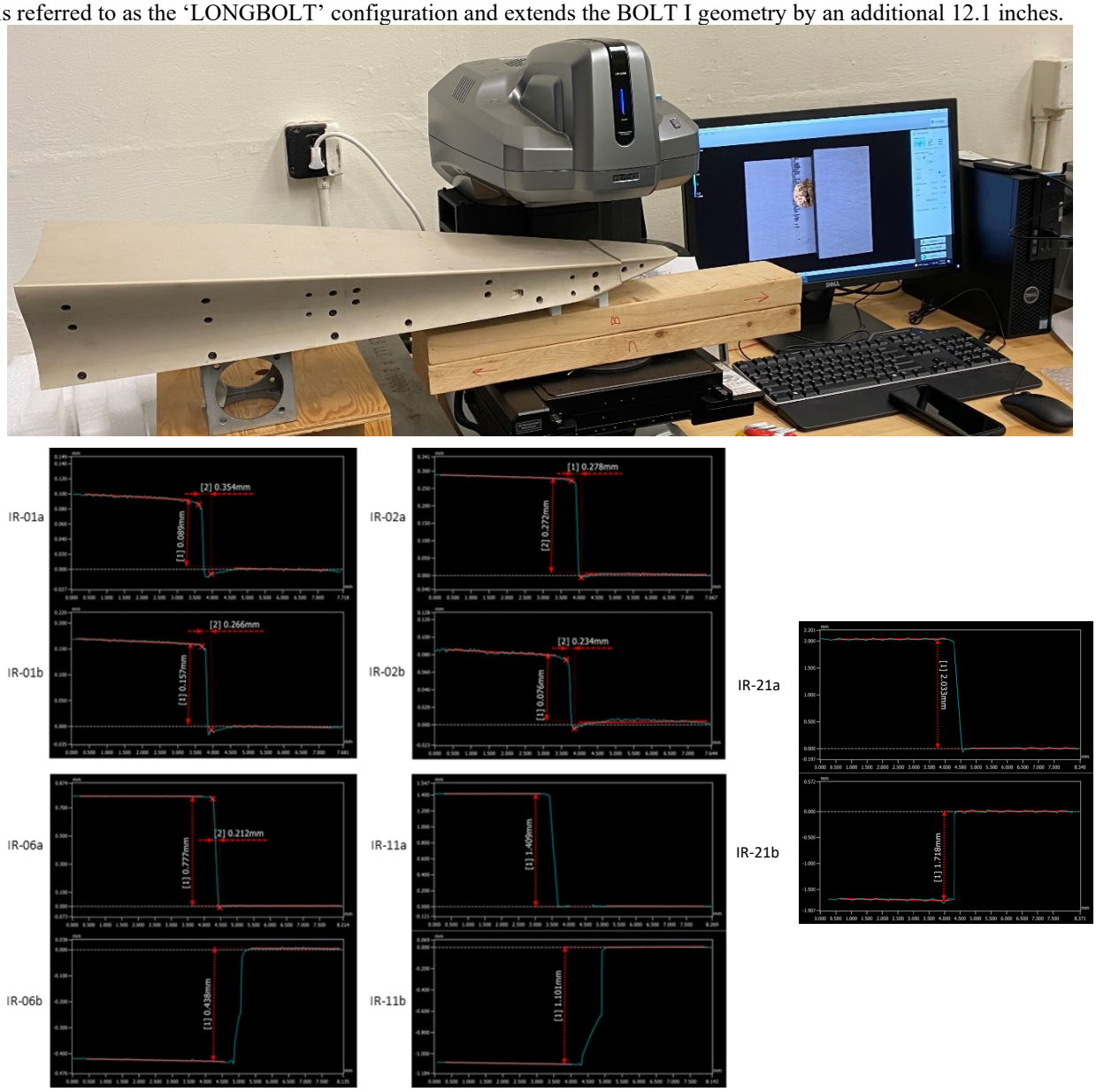

Figure 3. (Top) LONGBOLT Configuration on the optical scanning microscope stage. (Bottom) Step height measurements made using an optical scanning microscope. All step height values were measured along the model centerline.

Step heights were measured using an optical scanning microscope, which uses visible light to measure 3D objects, as shown in Figure 3 (top). The optical scanner lists a height measurement precision of 3.94×10^{-5} inches. The intended range of step heights was ± 0.005-inches to ± 0.1-inches. The measured step heights of the assembled model, k_m, differ from the designed step heights, k_d, significantly. The primary cause of the difference is a slight deformation of the thin region of PEEK near the joint. As a result, the two smallest step inserts (IR-01 and IR-02) produced very small forward facing (FF) steps. All step height measurements were taken using multiple scans near the center line of the model. The step heights were noticeably different near the leading edge compared to the centerline. The baseline step height, k_B, of 0.005-inches is used as a reference for the other measured step height values. Some of the resulting step heights generated by the various insert configurations are shown in Figure 3 (bottom) and given in Table 2.

Table 2. Step Height Values for As-Built Configurations

BST Insert	Step Direction	$k_{Measured}$ (mm)	$k_{Measured}$ (in)	Baseline % (k_B=0.005-in)
IR-21b	RF	1.718	0.0676	13.5 k_B
IR-11b	RF	1.101	0.0433	8.7 k_B
IR-06b	RF	0.438	0.0172	3.5 k_B
IR-02b	FF	0.076	0.0030	-0.5 k_B
IR-01a	FF	0.089	0.0035	-0.7 k_B
IR-01b	FF	0.157	0.0062	-1.2 k_B
IR-02a	FF	0.272	0.0107	-2.1 k_B
IR-06a	FF	0.777	0.0306	-6.1 k_B
IR-11a	FF	1.409	0.0554	-11 k_B
IR-21a	FF	2.033	0.0800	-16 k_B

C. Computational Data

The numerical results presented in this paper were computed using The Langley Aerothermodynamic Upwind Relaxation Algorithm (LAURA) [9]. LAURA is a finite-volume shock-capturing structured-grid computational fluid dynamics (CFD) tool specialized for hypersonic reentry flows. Either the Euler, thin-layer Navier-Stokes, or full Navier-Stokes equations are relaxed in pseudotime to a steady state. First-order inviscid fluxes are constructed using Roe's flux difference splitting with Harten's entropy fix and are extended to second-order using Yee's Symmetric Total Variational Diminishing (STVD) limiting. Second-order central differences approximate the viscous fluxes. LAURA can utilize point or line-implicit relaxation and employs MPI to run efficiently on parallel computing architectures. The solutions used for comparison to wind tunnel data were created using the same mesh refinement principles explored in [10] by Rieken et al. The Fay-Riddell values used to non-dimensionalize the heat transfer calculations are provided in Table 3.

Smooth OML (no step) cases were run for Re_∞ = 1, 2, 4, 5.6, and 8 x 10^6 / ft and the h/h_{FR} nondimensionalized heating values were extraceted from CFD solutions generated for each case by F. Greene. A BLAYER file is a LAURA output file written in .dat format that contains surface, edge, and boundary layer property data, from which the Re_θ reference values will be extracted for each flow condition. No uncertainty values are provided for the CFD data, and a detailed analysis of the CFD solutions is beyond the scope of this investigation. The CFD results are used as a baseline for initial assessment of the IR thermography technique and the validity of the IR data reduction process.

Table 3. Fay-Riddel Heat Transfer Coefficients for CFD Comparisons

Re_∞ $\times 10^6$ ft^{-1}	h_{FR} lbm/ft^2-sec	h_{FR} kg/m^2-s
1.05	0.1404	0.685473
2.04	0.20853	1.018103
4.06	0.28094	1.371629
5.65	0.33753	1.647917
7.97	0.38306	1.870208

D. Data Collection with Infrared Thermography

The use of infrared thermography (IRT) in the NASA Langley Aerothermodynamics Laboratory facilities is not new, but recent advancements in IR sensor technology have led to a renewed interest in and subsequent effort to develop an enhanced IRT test technique for hypersonic wind tunnel applications. Legacy facility hardware allows for the measurement of broadband long-wave infrared (LWIR) radiation with sufficient signal-to-noise for the calculation of heat transfer using absolute surface temperature. A state-of-the-art camera was used to collect calibrated temperature images. The primary components of the IRT system include a FLIR SC6701sls LWIR camera with 50mm lens, Zinc Selenide (ZnSe) window with anti-reflective coating which passes LWIR wavelengths from 8 – 12 μm, and the FLIR proprietary camera control and data acquisition software.

The FLIR camera was calibrated with NIST-traceable blackbody calibration sources at the FLIR calibration facility in Nashua, NH. Confirmation of the calibration and stated temperature accuracies were tested on site at NASA Langley using a Mikron M360 blackbody calibrator with a stated emissivity of 0.98 ± 0.01 and the ZnSe window placed between the detector and the blackbody source. A model of the relative spectral response transfer function η was derived analytically using a non-linear least squares regression of temperature T_b to sensor counts $S(T_b)$ with n=5. The results were combined with the stated temperature accuracies and noise equivalent differential temperature (NEDT) values to derive a model of the type 2 uncertainty parameters. A sensitivity analysis was also conducted for the determination of a weighting function for the uncertainty parameters for each input to the temperature extraction and heat transfer calculations. Details of the temperature extraction process are provided in the following subsections.

The factory calibration of the IR camera was conducted for two integration times yielding two calibrated temperature ranges: −4°F to 302°F (– 20°C to 150°C) and 131°F to 662°F (55°C to 350°C). Typical surface temperatures reached in the LAL 20-Inch Mach 6 tunnel can range from 65°F (30°C) during the pre-heat phase to around 475°F (246°C) at the stagnation point or leading edges during wind-on conditions. The standard IHEAT data reduction software package requires two temperature images to calculate the heat transfer for a given model material. Model surface thermographs were collected using the same factory calibration settings for wind-off and wind-on conditions, then the expanded calibration coefficients were applied to generate temperatures from the recorded raw signal in digital numbers (counts). Thorough explanations of the radiation equations and their treatment for IR thermography are provided by Wolfe and Zissis[11] and Minkina and Dudzik [12]. Details of the Planckian version of the Sakuma-Hattori model used in the development of non-linear calibration coefficients, and the subsequent uncertainty analysis for the heat transfer values generated by IHEAT are included in the following sub-sections.

1. Thermal Radiation

Radiative heat transfer is the exchange of heat by electromagnetic radiation. Infrared thermography refers to the use and detection of electromagnetic radiation with wavelengths ranging from about 0.1 μm to 20 μm to determine the surface temperature of an object. The wide range of IR wavelengths is subdivided into smaller bands with commonly used nomenclatures: near or NIR, short-wave or SWIR, mid-wave or MWIR, and long-wave or LWIR. Kirchhoff's law of thermal radiation refers to wavelength-specific radiative emission and absorption by an object in thermodynamic equilibrium. A perfectly efficient radiation emitter, known as a blackbody radiator, in thermodynamic equilibrium absorbs all light that strikes it, and radiates energy according to Planck's function. The Planck radiation law for a perfectly efficient radiator (eq1),

$$\boldsymbol{L}_b(\lambda, T) = \frac{1}{\lambda^5} \cdot \frac{c_1}{e^{\frac{c_2}{\lambda T}} - 1} \tag{1}$$

describes the relationship between an object's absolute temperature and the distribution of energy emitted from its surface in terms of unit area, time, and wavelength where c_1 and c_2 are the first and second spectral radiation constants, respectively. Here, the quantity L_b is referred to as the spectral hemispherical emissive power, or spectral radiance, of a blackbody emitter. The radiation constants are given in terms of Planck's constant $\boldsymbol{h}$, Boltzmann's constant $\boldsymbol{k}$, and the speed of light c_0 to yield (eq4).

$$c_1 = 2\pi \boldsymbol{h} c_0^2 = 3.742 \cdot 10^{-6}\, Wm^2 \tag{2}$$

$$c_2 = \frac{\boldsymbol{h} c_0}{\boldsymbol{k}} = 1.439 \cdot 10^{-2}\, m^2 K. \tag{3}$$

The total radiated energy may be found by integrating Planck's equation over the entire electromagnetic spectrum to obtain the Stefan-Boltzmann law, given by (eq5).

$$\boldsymbol{L}_b(T) = \int_0^{\infty} \frac{1}{\lambda^5} \cdot \frac{c_1}{e^{\frac{c_2}{\lambda T}} - 1} \, d\lambda \tag{4}$$

where the integrated function is called radiance. Modern IR detectors maintain relatively high spectral response only within a limited range of wavelengths. The in-band blackbody radiance measured by the detector then is given by (eq5).

$$\boldsymbol{L}_{b_D}(T) = \int_{\lambda_1}^{\lambda_2} \frac{1}{\lambda^5} \cdot \frac{c_1}{e^{\frac{c_2}{\lambda T}} - 1} \, d\lambda \tag{5}$$

Radiation observed from real bodies is always some fraction of the radiation expected from a blackbody at the same temperature because real bodies are not perfectly efficient radiators. Gray body is the term used for real objects which produce a constant spectral radiance but at a lower efficiency than a theoretically perfect blackbody. The in-band radiance emitted from a gray body is given by (eq5).

$$\boldsymbol{L}(T) = \varepsilon \cdot \boldsymbol{L}_b(T) \tag{6}$$

The ratio of gray body radiation to blackbody radiation for any given material is known as emissivity ε. The models used for hypersonic wind tunnel applications were assumed to behave as gray bodies and the determination of their emissivity is discussed in the following section.

2. Surface Emissivity Measurement

Qualitative IRT may be conducted for most surfaces with minimal effort, given the use of a sufficient detector and imaging software package for data acquisition. Quantitative IRT requires the accurate determination of emissivity for a given material if absolute temperature retrieval is desired. Kirchoff's radiation law (eq7),

$$\rho + \alpha + \tau = 1 \tag{7}$$

where the terms in ρ, α, and τ represent the reflectivity, absorptivity, and transmissivity coefficients of a given material, respectively, is applied to the test scenario. For a opaque media $\tau = 0$, the absorptivity and emissivity are equivalent and equal to $1 - \rho$. For the given temperature ranges and model conditions in this experiment, it is reasonable to assume Kirchoff's radiation law holds for the model and ZnSe window such that a simplified model of the emissive, reflective, and transmissive properties of the model, window, and atmosphere may be utilized. The wavelength-dependent transmissivity of the ZnSe window and AR coating is known from previous measurement and was measured again for this test by a method of ratios described in section 3. A mean value is used over the waveband of interest. An apparatus composed of a 4.0 x 6.0 x 0.5-inch machined aluminum block mated to a heating plate and a precision rotation stage was designed for the measurement and determination of the normal directional emissivity ε_n of the model material. Slots measuring 1.0 x 2.0 x 0.125-inch were machined into the face of the aluminum to allow placement of material coupons. The coupons were firmly secured to the aluminum block using flanges around the edges and thermal putty was used to esure uniform contact with the heating surface. Thermocouples were secured to both materials and the aluminum plate to verify the measured temperature from the IR data acquisition system. Small blackbody cavities were also machined into the aliminum surface such that their diameter to depth ratio produced an emissivity of 0.99. The cavities provided an additional data point for the observed temperature of the materials in the scene. While one side of the material sample was heated, the other was visible to the IR camera. The measurement was conducted with a well-known emissivity material (black electrical tape) applied to a PEEK coupon, in the same field of view as the un-coated PEEK. The uncoated PEEK material was measured to have an emissivity value of $\varepsilon_n = 0.91 \pm 0.005$ while viewing at a normal angle of incidence. Additional view angles were measured to verify the drop in emissivity, and those values were plotted against an emissivity model similar to the one described by Cerasuolo [13]. For viewing angles less than 45-degrees, the results well-matched with an analytical determination of the directionally-dependent emissivity function developed at LaRC using Kirchoff's law and the Fresnel equations to approximate perpendicular and parallel components of reflected radiation for dielectric materials. The emissivity

values for uncoated PEEK were then used as inputs to the analytical derivation of the directionally-dependent emissivity function (eq8). The emissivity function coefficients which fit the experimental data were found to be $\hat{\alpha} = 0.0255$ & $\hat{\beta} = 1.3345$.

$$\varepsilon_m(\theta) = \varepsilon_n \cos(\theta)^{\frac{\hat{\alpha}}{\cos(\theta\hat{\beta})}} \tag{8}$$

This emissivity function (Figure 4) was used to apply corrections for the emissivity variation across the surface of the model. For the BOLT viewing geometry all normal viewing angles are |0° – 30°| and therefore well within the constant region of emissivity, due to the model shape and test set-up. A range of 0.905 to 0.915 was used to define the uncertainty contribution.

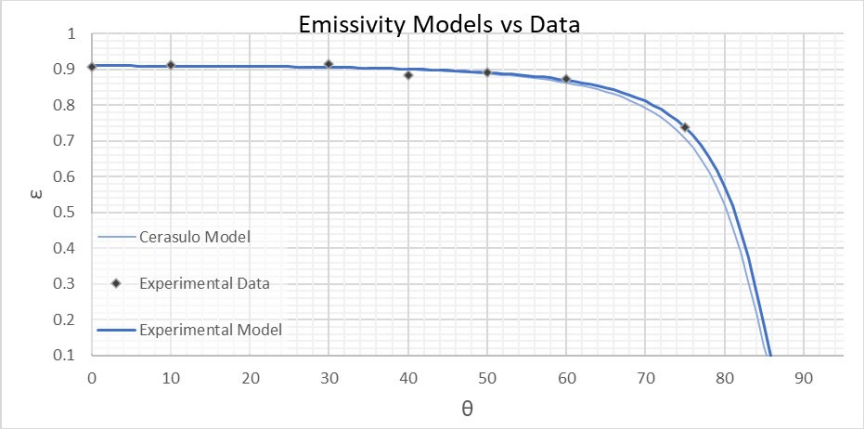

Figure 4. Directional emissivity function developed using experimental data.

3. Window Transmissivity Measurement

Window transmittivity, τ_w, was estimated by collecting images of a blackbody source in a lab setting. The camera and target were set a short distance apart sufficient to 'flood' the sensor with the signal from the calibrated source. Two sets of 100 images were collected of the blackbody target at 5 temperature settings spanning the range of temperatures predicted for the model surface. One data set at each blackbody set point was collected with the ZnSe window in the line of sight between the sensor and the target, while the other was taken without the window in place. Applying the method of ratios allowed for calculation of the windows transmissivity as a function of source temperature, as shown in Figure 5. No notieceable difference was measured when using either the 50mm or 25mm lens. It should be noted that the window was kept at a constant temperature during the measurements and did not experience the differential heating which occurs when it is installed in the 20-inch Mach 6 test facility.

$$S(T_i)_{win} = (\varepsilon_{bb} \cdot \tau_{win}) S_{bb}(T_i) \quad \Rightarrow \quad \frac{S_{bb}(T_i)_{win}}{\varepsilon_{bb} \cdot S_{bb}(T_i)} = \tau_{win} \tag{9}$$

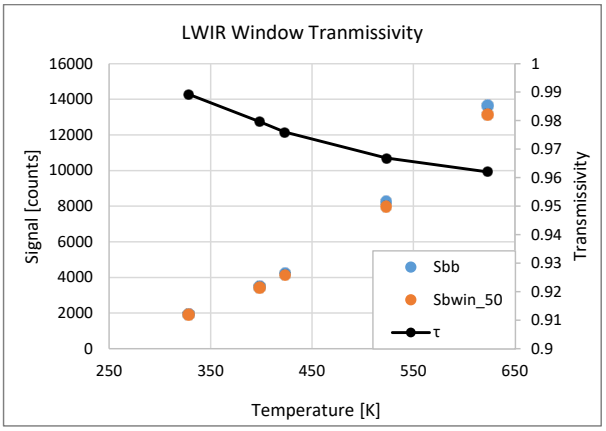

Figure 5. ZnSe IR window transmissivity measurement data.
Tranmission of the window ws obtained by the method of ratios.

4. Thermal Imaging

A camera system model was developed to quantify uncertainty parameters in the temperature image acquisition process. The thermal radiation arriving at the detector is modeled by the superposition of three signal components to provide a signal expressed in digital numbers, S, such that the total value S_{tot} may be expressed as a function of apparent temperature (eq10).

$$S_{tot} = S_a + S_w + S_m = F(T_{app}) \tag{10}$$

where

$$S_a = (1-\varepsilon_m)\cdot \boldsymbol{L}(T_a)\cdot\eta = (1-\varepsilon_m)\cdot F(T_a)$$
$$S_w = (1-\tau_m)\cdot \boldsymbol{L}(T_w)\cdot\eta = (1-\tau_m)\cdot F(T_w)$$
$$S_m = \varepsilon_m \cdot \boldsymbol{L}(T_m)\cdot\eta = \varepsilon_m \cdot F(T_m)$$

The subscripts a, w, and m represent the thermal radiation contributions from the ambient thermal environment (i.e. the test section walls), the ZnSe window, and the model itself. The non-linearity function η is intrinsic to the camera, and is approximated by plotting the reported radiance incident upon the detector to the digital numbers S, reported by the camera for a given calibration, given in arbitrary units of counts. Radiance is a non-linear function of temperature, but in narrow wavebands a linearization is desired so that any change in radiance from a source will produce a proportional change in the signal at the detector.

The use of a transfer function from apparent temperature to counts is employed for deconvolution of uncertainty terms and accurate temperature retrieval [12]. Signal values are relatively simple to work with and deriving the transfer function may be done empirically with a blackbody calibration source and the detector. A non-linear least squares regression was conducted to fit blackbody temperature values to counts from the detector. The Planckian form of the Sakuma-Hattori equation is employed to define and quantify the uncertainty factors associated with the temperature retrieval. The general Sakuma-Hattori equation in Planckian form and its inverse are given by (eq11) and (eq12).

$$S(T) = \frac{C}{e^{\left(\frac{c_2}{AT+B}\right)} - 1} + G \tag{11}$$

The empirical form used for calibrating the camera during this test includes variables for emissivity of the model, ε_m, and the transmittivity of the IR window, τ_{win}, and is given by (eq12). Very short viewing distance reduces the dependency of atmospheric transmission effects, so they are assumed to be included in the window transmissivity. The window transmissivity measurement also includes the detector's relative signal response as a function of wavelength. It was not practical to measure it directly, and all other measurements in the test are conducted over the full band of the detector's sensitivity region. These empirically derived calibration measurements are used to determine the appropriate inverse Sakuma-Hattori equation (eq12) for retrieval of the model surface temperature once suitable coefficients *A, B, C* and *G* are found. The measured coefficient values are given in Table 4.

$$T_m(S) = \frac{B}{ln\left(\frac{\varepsilon_m \tau_{win} C}{S_m - G} + A\right)} \tag{12}$$

This temperature value is taken at every pixel in the detector focal plane array, and an accurate temperature image can be produced using the resulting expanded sensor response calibration curve shown in Figure 6. The heat transfer equations are then performed on a pixel-wise basis, to form 2-dimensional heat transfer images. The heat transfer calculations are discussed in section the Experimental Results section.

Table 4. Calibration Coefficients

A	B	C	G
1.008	0.7235	6.368	1962.22

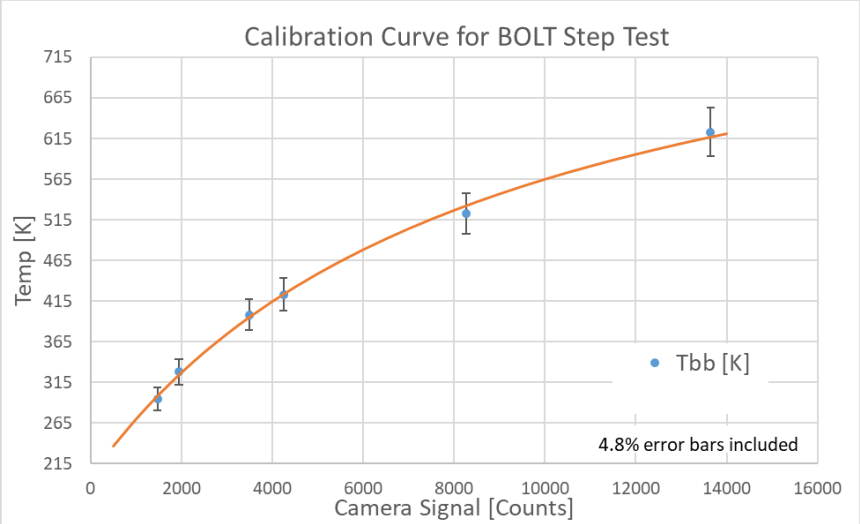

Figure 6. The sensor response across the entire dynamic range of the camera is non-linear, thus a Sakuma-Hattori model was used to conduct temperature retrieval.

5. Uncertainty Quantification

The uncertainty in temperature is determined by the inputs to the inverse Sakuma-Hattori equation and the measurements made to define those inputs and is given by the following equation:

$$\left(\frac{\Delta T_m}{T_m}\right)^2 = \left(\frac{\Delta S}{S}\right)^2 + \left(\frac{\Delta \varepsilon}{\varepsilon}\right)^2 + \left(\frac{\Delta \tau_{win}}{\tau_{win}}\right)^2 + \left(\frac{\Delta A}{A}\right)^2 + \left(\frac{\Delta B}{B}\right)^2 + \left(\frac{\Delta C}{C}\right)^2 + \left(\frac{\Delta G}{G}\right)^2 \tag{13}$$

Here the input terms to the temperature retrieval uncertainty quantification are the normalized standard deviations, in given by $(\Delta x_i / x_i)$, for each measured variable and are treated as type B uncertainties as defined by NIST in [14]. The assigned distribution types for each variable and associated coverage factor u_i is indicated in Table 5. Assuming the standard deviations of the measured input terms are uncorrelated, the treatment all the input terms as type B uncertainties provides a means to derive a total combined uncertainty from a non-uniform dimensionality of terms.

Table 5. Temperature Retrieval Uncertainty Values

			Uncertainty Quantification:		Temperature					
Value Ranges:						(H-L)/2	Ui / u	(ui/xi)	coverage factors:	
Variable	xi	*ui* distribution type	u-factor	Low	High	*Ui*	*ui*	ui (%)		k = 1.96
ε(θ)	0.91	log-Norm for θ: 0 to 30 de	2.375	0.898	0.920	0.011	0.004631579	0.51%		2-σ
τ_window	0.975	Square for xlow-xhigh	1.732050808	0.962	0.989	0.014	0.007881585	0.81%		95% C-I
A	1.00083	Triangle: xi ± 2%	2.449489743	0.976	1.026	0.025	0.010214641	1.02%		
B	0.72984	Triangle: xi ± 2%	2.449489743	0.712	0.748	0.018	0.007448905	1.02%		k = 3
C	6.28236	Triangle: xi ± 2%	2.449489743	6.125	6.439	0.157	0.064119081	1.02%		3-σ
G	1962.19041	Triangle: xi ± 2%	2.449489743	1913.136	2011.245	49.055	20.02652204	1.02%		99.7% C-I
S	Var(T)	Gaussian: use 3-sigma	3		uncertainty ΔS(T):	0.313%	k * std(S):	0.94%		
							Combined std Uc:	2.44%	2-σ Ue:	4.79%

These uncertainty terms are added in quadrature to determine a 2-σ (95.4% confidence interval) value for temperatures retrieved in the IR data acquisition process.

A similar approach was taken for estimating the uncertainty of the heat transfer calculations. Heat transfer calculations are done using the LaRC IHEAT data processing tool, developed at LaRC and described in [15]. The basic definitions of the convective heating film coefficient generated as output by IHEAT is given by (eq14), where the convective heating film coefficient and specific heat are represented by h, and c_p, respectively. The IHEAT algorithms developed by Merski et al. [16] were developed to utilize temperature-dependent material thermal properties of a given material during two-color phosphor thermography tests — typically Macor or fused silica — to determine the local value of h for all image locations based on temperature time-history. One important assumption made within the software is that adiabatic wall enthalpy H_{Aw} is equal to the total wall enthalpy, which may be less accurate for highly oblique shocks.

The same algorithms apply for IR data and thermoplastics, making the latest edition of the IHEAT software the default data processing code used by the Aerothermodynamics Branch at NASA Langley. The heat transfer uncertainty was quantified by Merski previously for phosphor thermography, and the inputs are similar for IRT. A significant advantage of IR thermography is the greatly reduced uncertainty in ΔT used to solve the heat transfer equation. A uniform distribution was given to the uncertainty values extracted from previous literature [16] for additional conservatism. Primary drivers for the uncertainty in heat transfer calculations are the uncertainties in temperature-dependent thermal property values, and the measured temperatures of the model. The inputs to the heat transfer uncertainty values (Table 6) are treated similarly to the temperature uncertainty values, described previously, and the total combined uncertainty in heat transfer is given by (eq15):

$$h \equiv \frac{q_{conv}}{(H_{AW}-H_w)} \qquad H_{Aw} \cong H_0 \equiv c_p T_\infty + \frac{U_\infty^2}{2}, \tag{14}$$

$$\Rightarrow \quad \left(\frac{\Delta h/h_{FR}}{h/h_{FR}}\right)^2 = \left(\frac{\Delta \mathrm{d}T_m}{dT_m}\right)^2 + \left(\frac{\Delta k_{PEEK}}{k_{PEEK}}\right)^2 + \left(\frac{\Delta C_{p_{PEEK}}}{C_{p_{PEEK}}}\right)^2 + \left(\frac{\Delta H}{H}\right)^2 + \left(\frac{\Delta h_{F-R}}{h_{F-R}}\right)^2 + \left(\frac{\Delta t_{eff}}{t_{eff}}\right)^2 \tag{15}$$

Table 6. Heat Transfer Uncertainty Values

			Uncertainty Quantification:		Heat Transfer		
iHEAT Value Ranges:				or		Bounding %	
Variable	xi or xavg	Δxi or std(xi)	*ui* distribution type	u-factor	k-value	*Ui*	ui
k_PEEK (Elora)	0.28462	0.03514	Uniform u=sqrt(3)	1.732050808	1.96	12.35%	13.973%
Cp_PEEK	1.60944	0.09880	Uniform u=sqrt(3)	1.732050808	1.96	6.14%	6.947%
dT (Ttr-Tpr)	2*Ue(T)	0.04785	Combo (see above)		1.96	9.57%	9.571%
H_aw		6.00%	Normal		1.96	6.00%	6.000%
t_eff		2.50%	Uniform u=sqrt(3)		1.96	2.50%	2.500%
F-R coefficient	3.76%	0.101%	Uniform u=sqrt(3)	1.732050808	1.96	0.06%	0.115%
					2-σ Combined Standard Uc:		19.43%

V. Experimental Results

A. Raw Infrared Data

The FLIR camera was equipped with a 50mm Ge lens and set to a capture rate of 60 Hz with an integration time of 38.56 µs, such that frame 300 represents the model being in the Mach 6 flow for approximately 5 seconds. This time was chosen after an analysis of surface thermal emission dependence on time in the flow. Nominal practice in the LAL facilities is to define the time of 'temporal collapse' as the minimum time within the flow for the surface heating to reach a steady state, before 3D conduction effects are observed. The assumption is that the temporal collapse time is Reynolds number independent when normalized via Eq. 14. The data are then compared to CFD solutions to determine if the results are anomalous or well-behaved.

The IR data were also used to extract approximate spatial calibration values for the model in the scene. The step dimension is the primary spatial calibration source, as its x/L value is well known. Additionally, the width of the joint at the step is a constant, regardless of any slight movement of the model, and the distance $-1 < y/y_{ref} < +1$ provides a

good metric for analysis of the laminar to turbulent transition location for the prominent transitional 'lobes' commonly observed on the BOLT geometry. Thus, y00 and y50+ are used to denote the axial line cuts along the centerline and at 50mm from the centerline, respectively, throughout the analysis. For simplicity, y50+ is also used as y_{ref} such that $y/y_{ref} = 1$ is equivalent to the y50+ location. A subset of the test data, illustrating the relative effects of both changing step height and Reynolds number are presented in Figure 7 and Figure 8 for qualitative review. Initial runs targeted Reynolds number sweeps from 8 million/ft to 1 million/ft. As the test progressed, the research team became more interested in the lower Reynolds number cases, and a decision was made to forego the 6.5 million /ft runs to allow more experimentation of different nose configurations. The step configurations are denoted by the relation to the

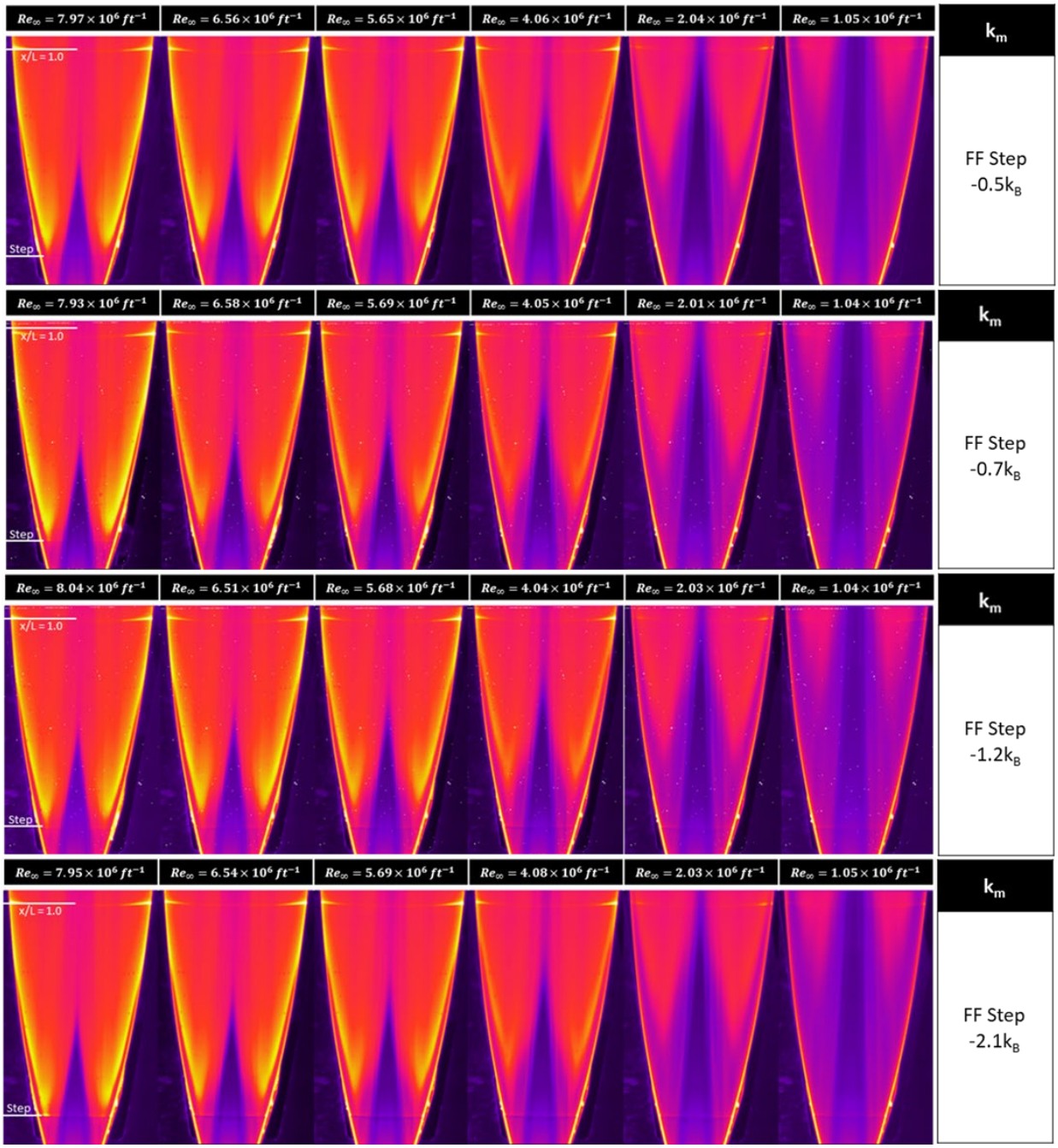

Figure 7. Raw IR output shows surface temperature rise in false color. The transition lobes are readily apparent. Reynolds number sweeps from 8 x10^6 /ft to 1 x10^6 /ft were performed for a variety of step configurations. The step heights for each Reynolds number grouping are included to the right.

defined baseline step height k_B = 0.005-in. Negative or positive values are used to identify the directionality of the step face – either FF or RF – with respect to the flow. Negative values of step height (e.g. -1.2k_B) indicate a forward facing step. The closest value to a '0-step' case was given by the -0.5k_B configuration, and a representative image for that case at the highest Re are presented in Figure 8 as a reference. The highest Renolds number is provided as a reference image to show the maximum heating for a 0-step case. Figure 9 shows representative schieren images of the shock structures associated with FF and RF steps in comparison to the "no step" configuration. Model curvature makes these qualitative only, as some details of the shock structures near the centerline are occluded due to the

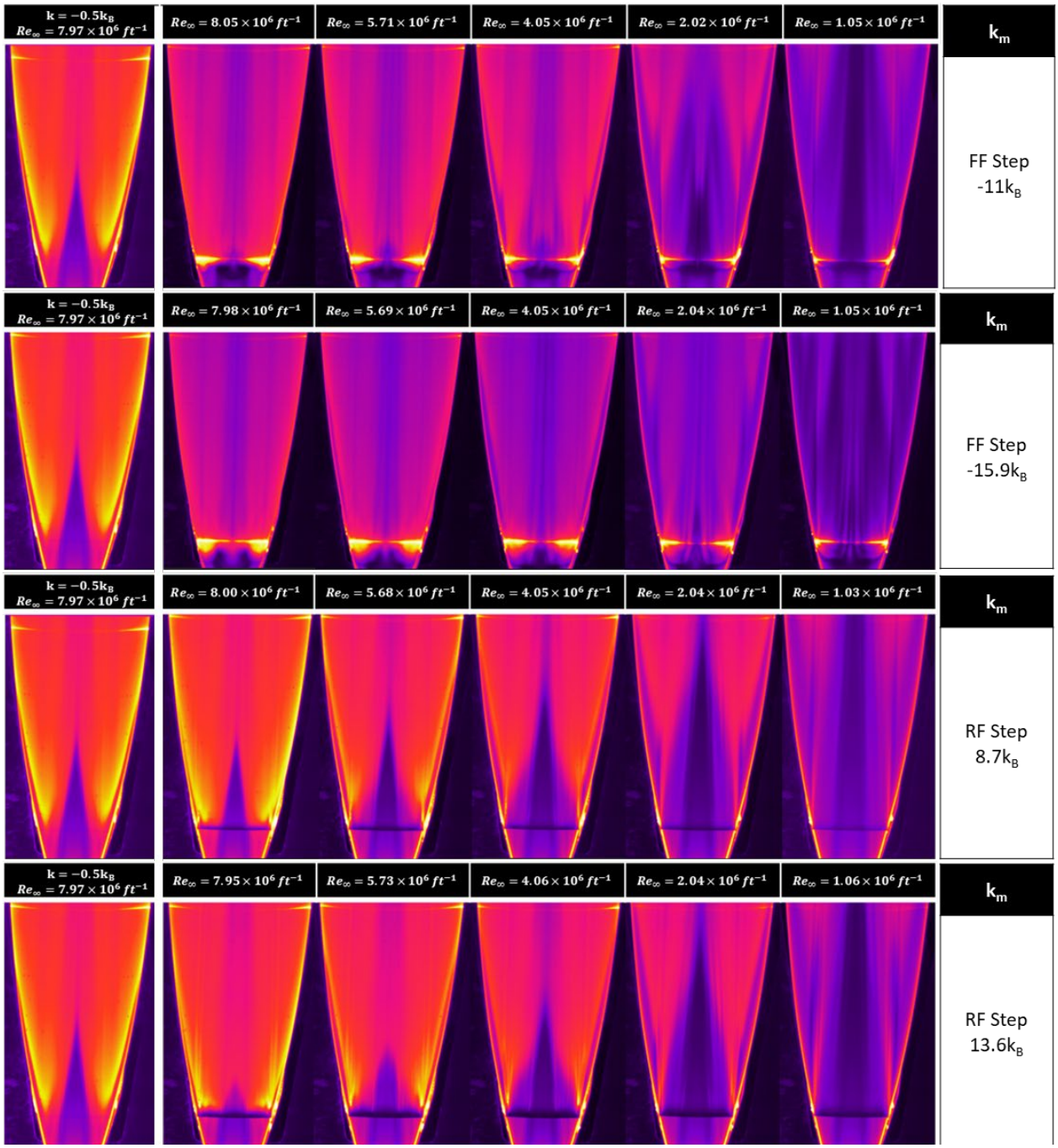

Figure 8. Raw IR output shows surface temperature rise in false color. Reynolds number sweeps from 8 x10^6 /ft to 1 x10^6 /ft were performed for a variety of step configurations. Reference image of the -0.5k_B case at $\boldsymbol{Re}_\infty = 8$ million per ft. is shown to the left of each sequence to show the maximum heating result of a 0-step case.

concavity of the model. The use of a Flat-BOLT design would enable a more thorough analysis of these structures to compare with the thermograms to better understand the environment near the step and downstream. All test entries were conducted at $\alpha = \beta = 0$-deg.

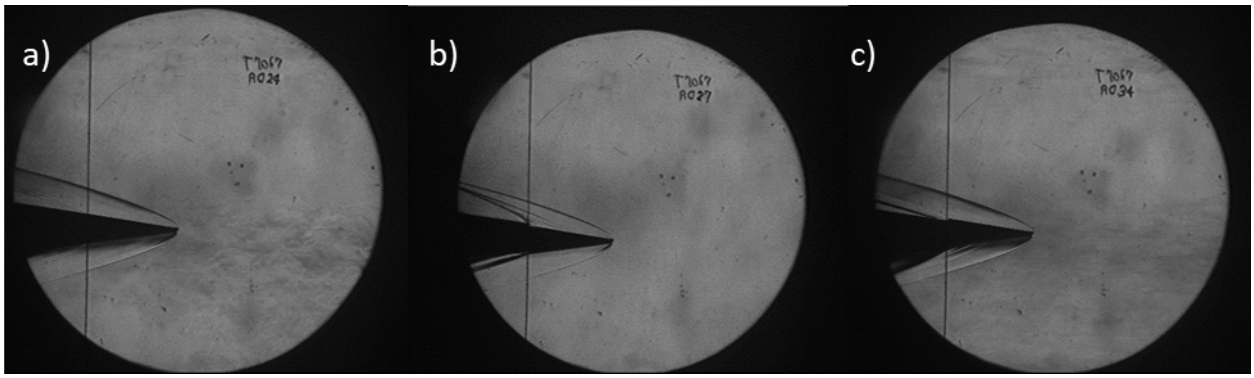

Figure 9. Schlieren photography showing the shock structures resulting from a) -0.5k_B, b) -16k_B, and c) 13.6k_B

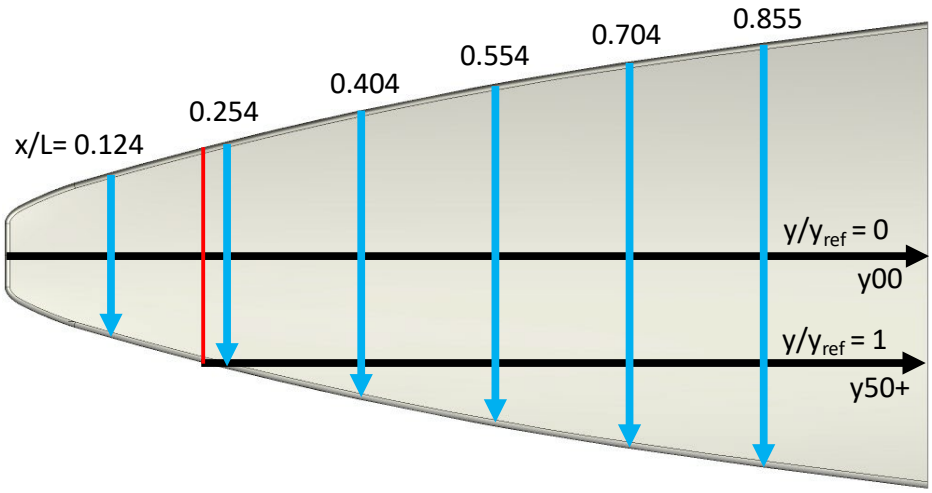

Figure 10. Line Cut locations depicted on a BST model CAD. Red line represent the step location x/L= 0.21. Blue lines represent the spanwise x/L cut locations. Black lines represent the lengthwise cut locations at y/yref = 0 and 1.

B. Heat Transfer Data

The heat transfer data extraction method goes as follows: 1) define calibration coefficients of the Sakuma-Hattori equation for a single integration time of the camera over the range of expected temperatures; 2) export the raw couts from the IR software for a pre-run frame and at frame 300 during the test entry; 3) a apply calibration equation to all pixels to get the transfer from Counts > Temp(K) > Temp(C) then export as .csv files; 4) import the temperature .csv files to IHEAT for processing to heat transfer and non-dimensionalize using BOLT Step model nose radius of 0.0935-in to generate Fay-Riddell film coefficient reference values; and finally 5) extract line cuts along regions of interest using the built-in IHEAT profiling tool. The surface heating calculations generated by IHEAT are normalized by a reference film coefficient value derived from the Fay-Riddell correlation for stagnation point heat flux. The IHEAT software package uses a wall temperature reference of $T_w = 300K$ to generate the Fay-Riddell reference film coefficient value h_{FR}. The heat transfer data presented here are limited to $Re_\infty = 2 \times 10^6$ /ft and 4×10^6 /ft cases. Global heat transfer images are provided for comparison and set at a uniform scale with an upper bound of 0.05 h/h_{FR}. Nondimensionalized heat transfer data were extracted along longitudinal and spanwise directions and are presented in Figure 10. The primary goal of this experiment is to determine a relationship between the step height and onset of boundary layer transition. One approach currently being explored is determining the x/L location of the forward-most

'tip' of the heating lobes on either side of the centerline. These roughly align with the y/y_{ref} =1 location. Further analysis is required to establish a relationship between step height k and Re_θ, however, interesting trends do appear in the initial analysis of the heat transfer images.

Figure 11 shows examples of the conversion of raw IR counts to heat transfer images. The colorbar scale is in non-dimensionalized units of heat transfer and is valid for the lower row of images. While heat transfer may be qualitatively inferred from the raw IR imagery, it does not provide the whole story. For instance, inferring transition onset locations from the signal count data is approximate until the data can be converted to heat transfer, establishing the nominal laminar heating levels to allow accurate indication of the deviation locations. The onset of transition can be more accurately defined from the line cut data by locating the spatial location (typically x/L) where the heating levels rise significantly above the measured and predicted laminar heating rates. Thus, in Fig. 11, the line cut locations that are presently used to better capture the transition onset movement are indicated by the black dashed lines on the lower right image. Figure 12 provides a comparison of the test data taken for a no-step condition ($-0.5k_B$) for a sweep of Reynolds numbers. The measurement data show good agreement with the smooth OML laminar CFD data along the centerline which suggests the validity of the IRT methodology, however better agreement is expected near the forward leading edge. One likely explanation is the slight distortion of x/L for the model in the IR imagery vs. the CFD. The IR imagery is slightly skewed due to the camera view angle, and no corrections were made via 3D mapping the image to the model surface in this preliminary assessment.

Transition onset locations can be easily seen in Fig. 12 as the x/L location that corresponds to the location of the initial deviation from the predicted laminar heating levels. Spanwise cuts are also provided in Figure 13 to show the heating across the model for a sample of x/L axial stations at constant a Reynolds number of 2 million/ft. The qualitative comparison to laminar CFD solutions shows generally good agreement, but the experimental data highlight the impact of the transition lobe structures on the surface temperature distribution. The appearance of these transition lobes is ubiquitous in other BOLT test data in non-quiet tunnels. The intersection of the transition lobes at the centerline produces the apparent uptick in heating past about x/L=0.5. One interesting question to explore will be the consistency of the lobe shape with increasing Reynolds number, and whether that can be used as an additional metric in the final analysis is still to be determined. The y/y_{ref}=1 data are below the fully turbulent CFD predictions for that region, but do show the effects of Reynolds number on the lengthwise location of boundary layer transition. The data from this cut location will be used as a primary input in the final data assessment to examine the effects of 2D steps in tht region, for all runs because it appears well aligned with the forward 'tip' of the transition lobe formation.

The composite image in Figure 14 shows a series of line cuts along the centerline and y/y_{ref}=1 locations for a variety of step conditions while holding Reynolds constant to show the effects of step height on transition. The global heating images are shown below it for reference. One can observe in Fig. 14 that the larger FF steps are disruptive such that augmented heating is seen in front of the step and even on model centerline. It is likely that 3D temperature conduction effects are a contributing factor. Conversely, for the RF steps shown, no significant effects are seen at Re_∞= 2 million/ft on CL, while there is some forward movement on transition onset observed in the y/yref=1 data. Figure 15 examines the additional impact of increasing Reynolds number for the centerline and y/y_{ref} = 1 data for a smaller set of step configurations for a Reynolds number of 4 million/ft. This figure mainly focuses on the effects of the larger FF and RF steps. Transition onset locations are already nearly up to the step location at y/yref=1 location at this Reynolds number, but some additional impact of these larger steps are still seen. Figure 15 illustrates the centerline and y/y_{ref} = 1 data for a sweep of step configurations while holding Reynolds number constant at 4 million/ft clearly indicating the effects of large FF and RF steps. Further comparison between the 2 million/ft and 4 million/ft cases is illustrated in Figure 16, which shows spanwise cuts for a sample of FF and RF step heights ($-0.5k_B$, $-11k_B$, and $8.7k_B$) at three x/L stations.

Additional analysis of Figure 16 provides some confirmation that a RF steps produce noticeably reduced surface heating downstream from the joint. Centerline region shows consistency in heating values for both RF step configurations ($-0.5k_B$ & $-11k_B$) at both Reynolds numbers, indicated by the dashed lines and lighter colored lines. The 2 milliion/ft case includes strong gradients across the span of the vehicle acreage down wind of the joint for all FF and RF step configurations, while the 4 million/ft condition results in a more evenly distributed heating pattern as evidenced by the 0.704 line cut. Forward facing steps of sufficient height appear to more evenly distribute the heating across the acreage.

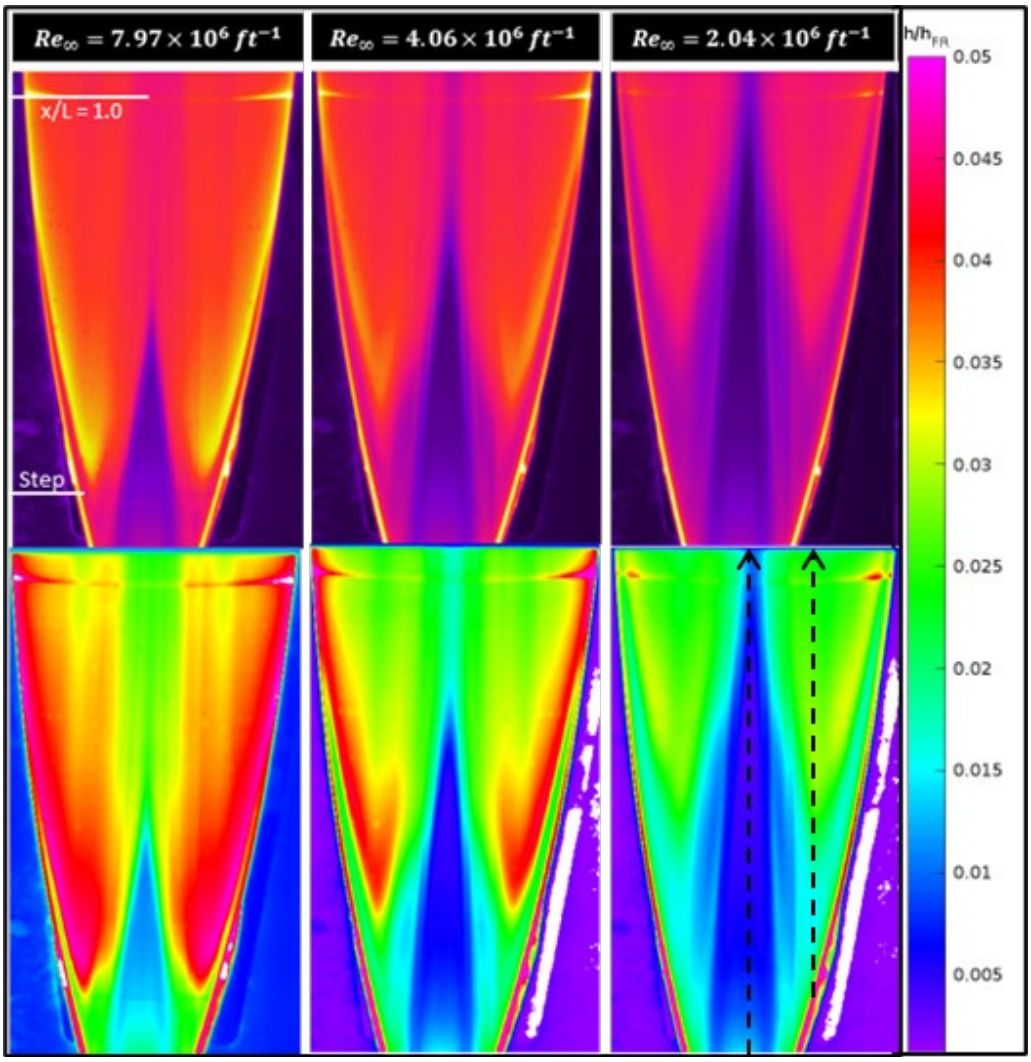

Figure 11. Raw IR images (top) and the resulting heat tranfer images (bottom) for $\boldsymbol{Re_\infty \approx 8,\ 4,\ 2 \times 10^6\ ft^{-1}}$ runs with k = -0.5k_B. Colorbar values are for the heat transfer images only (bottom row).

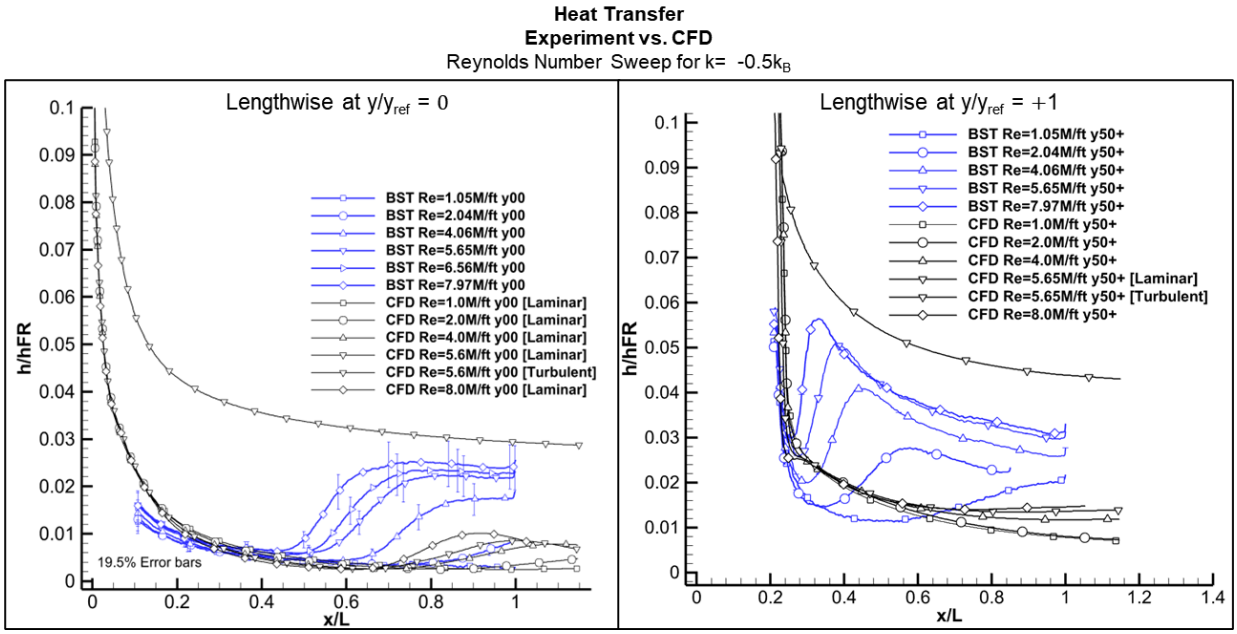

Figure 12. Reynolds number sweeps for k = -0.5kB. Cuts taken along the centerline (y00) and at y/yref = 1 (y50 +) provide a baseline for expected transition behaviour as a function of Reynolds number.

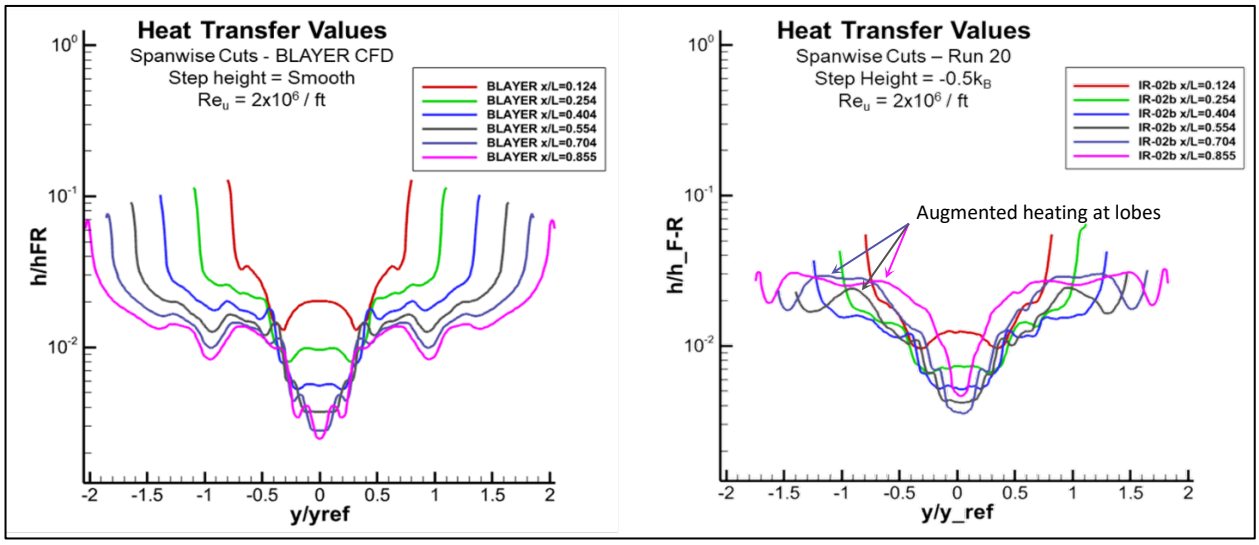

Figure 13. Spanwise cut comparison between the LAURA output (BLAYER) and the BST data**.** Heating augmentation at the transition lobes can be seen in the test data for stations with x/L $\geq$ 0.5.

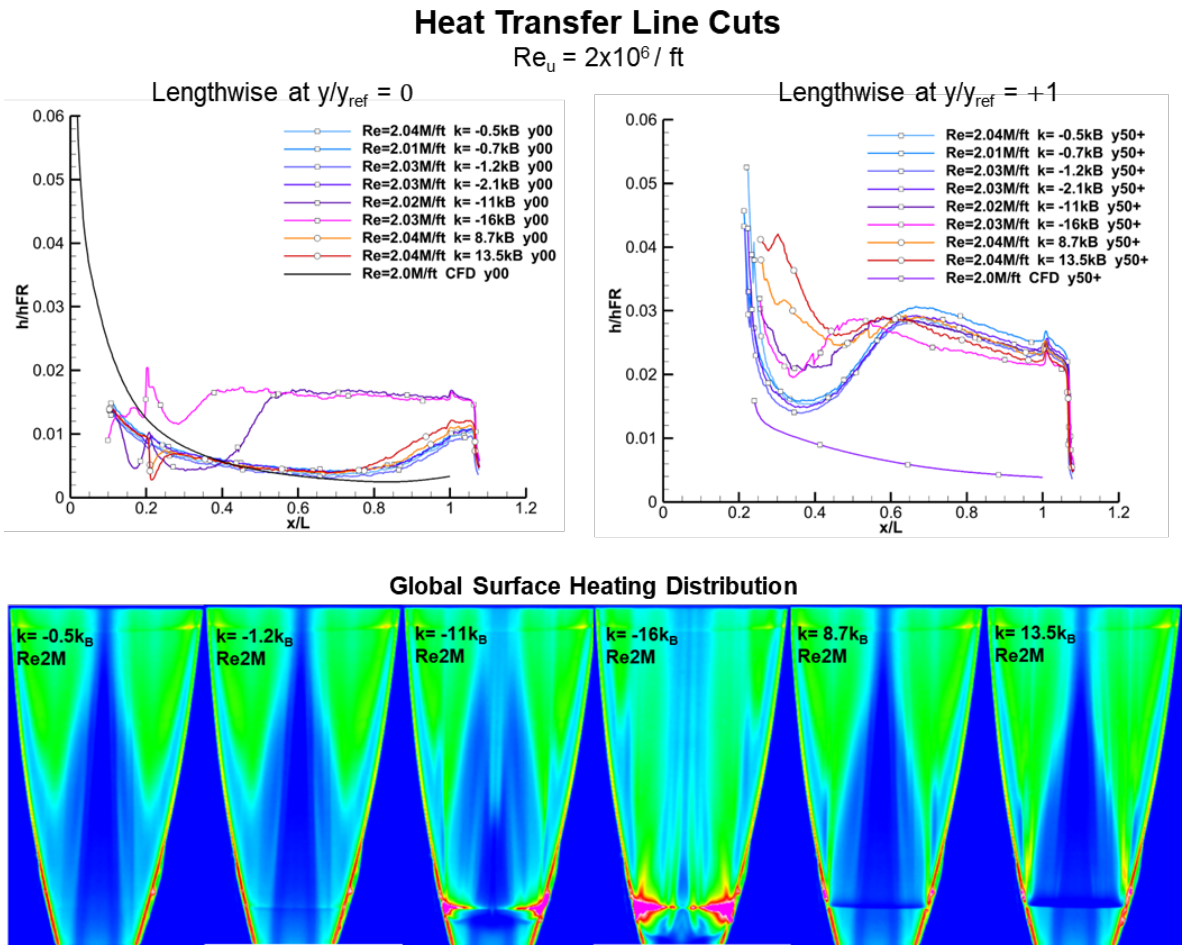

Figure 14. Step height sweep for $\boldsymbol{Re_\infty = 2 \times 10^6}$. Cuts taken along the centerline (y00) and at y/yref = 1 (y50+) provide insight into transition behaviour as a function of step height k.

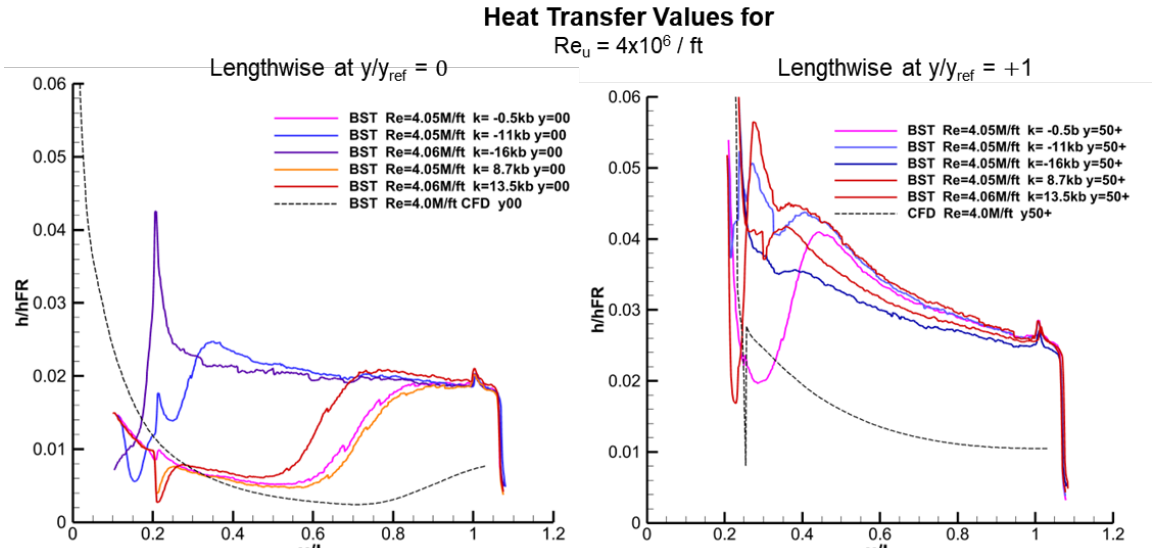

Figure 15. Step height sweep for $\boldsymbol{Re_\infty = 4 \times 10^6}$. Cuts taken along the centerline (y00) and at y/yref = 1 (y50+) provide insight into transition behaviour as a function of step height k. Laminar smooth OML CFD solutions provided for reference as black dashed line.

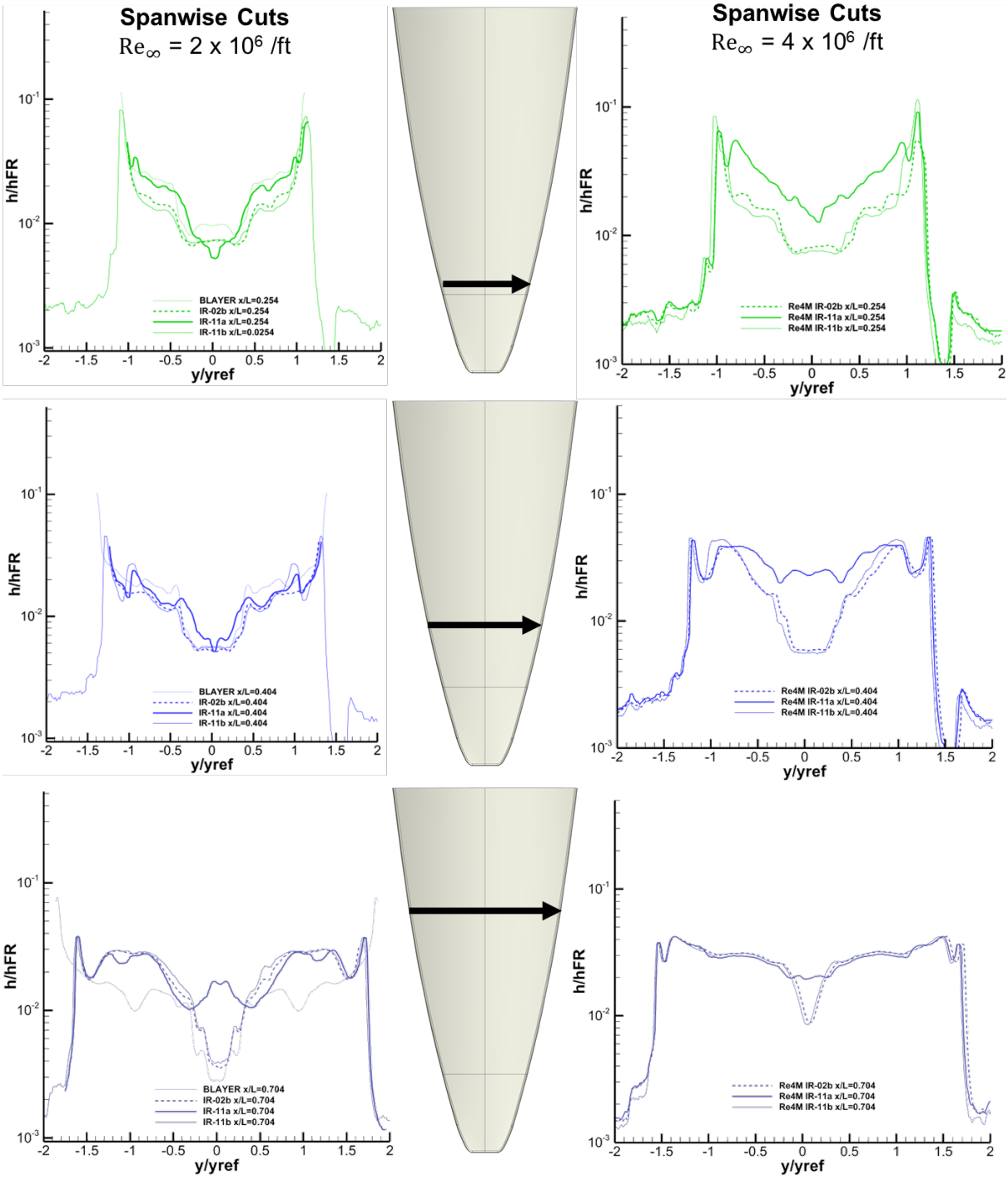

Figure 16. Spanwise cuts for $\boldsymbol{Re_\infty = 2 \text{ and } 4 \times 10^6\ ft^{-1}}$ cases with step heights of -0.5k_B (IR-02b), -11k_B (IR-11a), and 8.7k_B (IR-11b). Spanwise locations are depicted in the center of the figure.

VI. Discussion

Preliminary results provided here suggest that machinable thermoplastics such as PEEK can be used for quantitative aerothermodynamic analysis within the NASA Langley Aerothermodynamics Laboratory's 20-inch Mach 6 test facility via infrared thermographic data measurement techniques. Special attention should be paid to the thermal properties of the model material, and the measurement techniques employed to identify temperature-dependent thermal properties of any material intended for use with IR thermography. The uncertainty quantification process highlights the impact of uncertainty in thermal properties to the overall uncertainty in heat transfer calculations. Modern IR sensor technology enables significant improvements in heat transfer analysis by reducing uncertainty associated with the surface temperature measurements. A fully realized 3D mapping methodology, which can properly assign directionally-dependent emissivity values to a surface prior to the temperature extraction process, is also required for more complex geometries. One potential method for reducing the requirement for well-known surface emissivity functions could be realized with dual or multi-band thermography by using two or more sufficiently separated IR bandwidths to find a ratio of the emitted radiance.

Analysis of the full dataset is still ongoing with the intention of being published separately via a series of technical publications. One observation from the current analysis is that transition onset is observed coming from the leading edge (LE) region of the joint, which suggests the region is the most sensitive to step effects (see Figures 11, 12, 18).

Table 7. Approximate transition onset locations for k= -0.5k_B as a function of Reynolds number.

Re_∞ $\times 10^6$ ft^{-1}	CL x/L	y50 x/L
7.98	0.47	0.26
6.56	0.52	
5.65	0.57	0.28
4.06	0.66	0.3
2.04	0.85	0.34
1.05		0.56

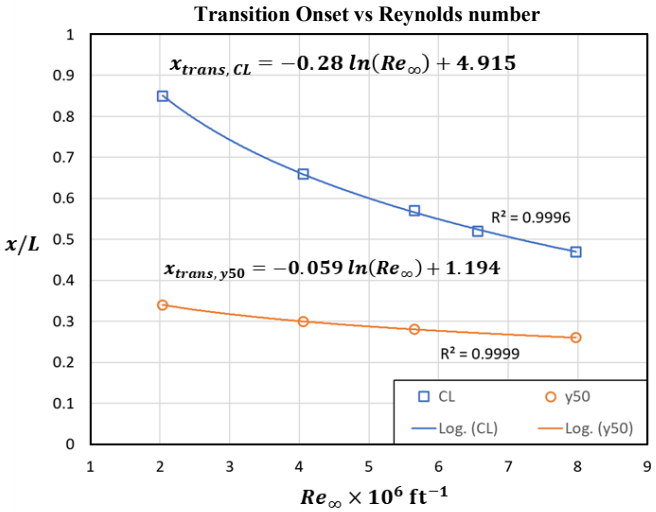

Figure 17. Transition onset locations as a function of Reynolds number for k= -0.5k_B.

Approximate transition locations as a function of Reynolds number for the no-step condition are given in Table 7, and shown in Figure 17. The relationship defined by Table 7 will be used as a baseline for comparing step effects for different configurations.

Much of the initial analysis presented thus far is focused on the flatter geometry near centerline and a follow-on activity should be the determination of step sizes for each LE, to augment the CL data. Initially, the laminar to turbulent transition was only measured along the centerline, but upon completion of the initial set of Reynolds number sweeps it was apparent that step height variations generated high heating the y/yref = ±1 location, where the step meets the leading edge. Additionally, significant differences in heat transfer are observed downstream of the step location for forward-facing and rearward-facing configurations (see Figures 15 and 16) . The FF step confirgurations show very high heating at the step location, but lower heating before and after the step and also a more distributed heating pattern downstream. Some flow recirculation of the boundary layer is suspected forward of the step, given a sufficiently large -k value. The RF step configurations show reduced heating immediately downstream of the step, which may indicate the separation and subsequent reattachment of the boundary layer in that region. The 3D recirculation area behind the joint also seems to culminate with a less pronounced heating streak again emanating from the LE. More work is required to differentiate the relative effect of the FF steps from the RF steps, but clearly the FF steps provide a more abrupt impact to the surface flowfield and BL development.

Additional work with the BST model design is being conducted by research partners at Raytheon Mission Systems and at other ground test facilities. Additional studies conducted in parallel with this effort included a Flat-BOLT model geometry, which allows for better shock structure analysis, an investigation of various nose shape impacts to boundary layer transition, and a series of discrete tripping configurations. A detailed comparison between BOLT Step model and Flat-BOLT will be presented in a follow-on analysis. Initial comparison is provided in the following section.

A. Flat-BOLT Experiment

The BOLT geometry, and in particular the modular BST model, provide an attractive testbed for the validation and maturation of high-speed vehicle design and analysis methods based on a fundamental research configuration with complex flow physics. Therefore, the original BST testing (above) inspired a second wind tunnel campaign as part of an agreement between NASA Langley and Raytheon, which occurred during June 2022 with Test 7072. This study was conducted using a modified, flattened version of the BST model, called the "Flat-BOLT" configuration. As discussed in an earlier paper [17], the planar top surface of the Flat-BOLT is generated by projecting the planform of the BOLT onto a 7-degree inclined flat plate. Thus, a compatible Flat-BOLT PEEK surface was manufactured to fit the same strongback as used in the BST model. Figure 18 shows a side-by side view of the BOLT and the Flat-BOLT skins with several nose shapes and step inserts. Removing the spanwise curvature from the top surface offers several advantages: 1) it isolates the effect of the planform shape on leading-edge and acreage heating (e.g., Figure 19 shows an alternate flat nose with a parabola shape), 2) it permits optical measurements of the boundary layer such as Focused Schlieren [18] and Focused Laser Differential Interferometry (FLDI), and 3) the Flat-BOLT acreage can host standard flat material coupons similar to the inclined flat plate model used in [19].

As a preview of the upcoming paper [20], Figure 19 provides a comparison the surface heating on BOLT and Flat-BOLT. The images in Figure 19*a* show the normalized surface heat flux for the BOLT and for the Flat-BOLT at two freestream unit Reynolds numbers. BOLT and Flat-BOLT exhibit very similar side lobes of increased heating associated with the onset of transition to turbulence and with the same shift forward as the Reynolds number increases. The magnitude of the heat flux increase in the lobes is slightly greater for the Flat-BOLT. A quantitative comparison of the normalized heat flux is provided in Figure 19*b.* along cuts at two spanwise locations for a series of test runs with successively increased Reynolds numbers. Along the model center, $y/y_{ref}=0$, the heat flux is in near perfect agreement for BOLT and Flat-BOLT, aside from a greater noise level for the Flat-BOLT[1]. Both models exhibit the same transition onset locations at the different Reynolds numbers. More noticeable differences are observed along the off-center cut location, $y/y_{ref}=1$. The transition onset is consistently farther forward for the Flat-BOLT, albeit not that significantly. Also, at the lower Reynolds numbers (Figure 19*a*), the normalized heat flux reaches a slightly higher level for the Flat-BOLT. Some of this may be impacted by the changing camera viewing angle for the curved BOLT surface and also due to slightly different perspective distortions of the images. Considering measurement uncertainty, heating for BOLT and Flat-BOLT appears to be in very good agreement. This is consistent with the CFD predictions from an earlier paper [17] that showed only minor differences between BOLT and Flat-BOLT in both laminar heat flux and in the linear growth rates for second mode and crossflow instabilities. A more detailed discussion of the results from the Flat-BOLT test will be provided in [20].

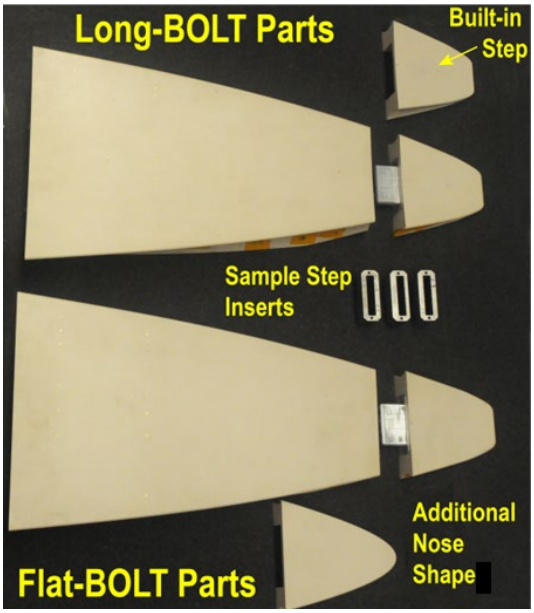

Figure 18. BOLT skin versus Flat-BOLT skin with sample step inserts and nose shapes.

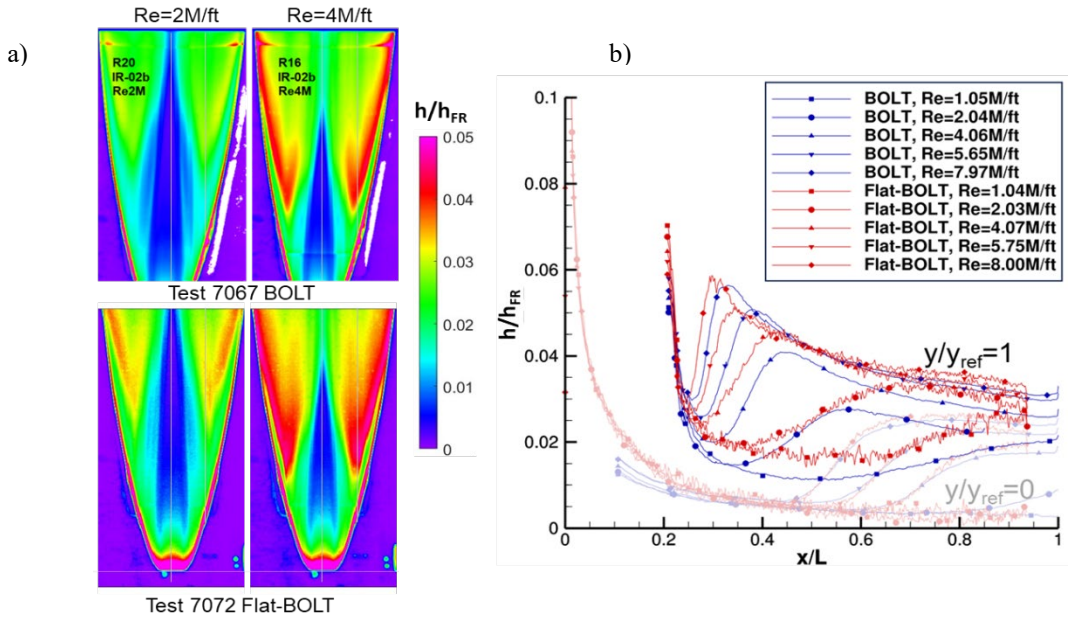

Figure 19. a) Normalized surface heat flux for two Reynolds numbers for BOLT (top) and Flat-BOLT (bottom); b) Normalized heat flux for several Reynolds numbers alond cuts at two spanwise locations. BOLT (blue) and Flat-BOLT (red).

VII. Summary

This report is an initial assessment of a new infrared thermography measurement apparatus in the Langley Aerothermodynamic Laboratory. The technique records global images of surface temperature and, through time-dependent conduction analysis, corresponding heat transfer rates. This measurement technique offers potential cost, manufacturability, and supply chain benefits over the legacy phosphor thermography technique, but with previously undetermined accuracy. Specifically, an investigation was carried out to explore how the height of forward-facing and rearward-facing two-dimensional steps and free stream Reynolds number affect the transition from laminar to turbulent flow on a 50%-scale BOLT flight test vehicle model in the LAL 20-Inch Mach 6 wind tunnel. This study involved 78 runs at Reynolds numbers between 1.4 and 11.3 million for various step heights. Data were collected using a develomental infrared thermography (IRT) technique, which included a FLIR SC6701sls LWIR camera and a Zinc Selenide window, to measure and analyze the heat transfer on the model's surface.

The IRT system's components were characterized to quantify their contribution to measurement uncertainty, resulting in a temperature measurement uncertainty of approximately 4.8% (2σ) and a heat transfer uncertainty of around 19.4% (2σ). These measurements were calibrated by applying an inverse Sakuma-Hattori equation for accurate surface temperature retrieval. The analysis revealed that while raw IR imagery provides qualitative heat transfer data, converting this data to heat transfer rates is essential for accurately determining transition onset locations. The onset is easily identified where heating levels rise significantly above predicted laminar rates, influenced by Reynolds number and step height.

Preliminary results indicate that forward-facing steps significantly disrupt the boundary layer, causing augmented heating at the step boudary and more evenly distributed surface heating downstream. Rearward-facing steps show reduced heating downstream, suggesting boundary layer separation and reattachment. Observations suggest the region near the leading edge and the joint is highly sensitive to step effects. Additional studies using a Flat-BOLT model showed similar heating patterns and transition behaviors to the BOLT model, aligning well with CFD predictions. Both models displayed increased heating at transition lobes, with slight variations in heat flux magnitude.

This report provides a preliminary assessment of the IRT technique used to acquire and reduce experimental data and to offer insights into the effects of FF and RF steps on boundary layer transition in Mach 6 flow. The ongoing analysis will be detailed in future technical publications.

References

[1] “BOLT II – Air Force Research Laboratory.” Retrieved 5 June 2024. https://afresearchlab.com/technology/bolt-ii/

[2] “Boundary Layer Transition (BOLT) | Johns Hopkins University Applied Physics Laboratory.” Retrieved 5 June 2024. https://www.jhuapl.edu/work/projects-and-missions/boundary-layer-transition-bolt

[3] Berry, S. A., and Carey F. Scott, J., “Experimental Aeroheating Study in NASA LaRC 20-Inch Mach 6 Air Tunnel: Discrete Roughness on BOLT – Test 7071,” NASA Technical Memorandum 20230003164, April 2023.

[4] Chynoweth, B. C., Edelman, J., Gray, K., McKiernan, G., and Schneider, S. P., “Measurements in the Boeing/AFOSR Mach-6 Quiet Tunnel on Hypersonic Boundary-Layer Transition,” presented at the 47th AIAA Fluid Dynamics Conference, Denver, Colorado, 2017. https://doi.org/10.2514/6.2017-3632

[5] Berry, S. A., Mason, M. L., Greene, F., King, R., Rieken, E., and Basore, K., “LaRC Aerothermodynamic Ground Tests in Support of BOLT Flight Experiment,” presented at the AIAA Scitech 2019 Forum, San Diego, California, 2019. https://doi.org/10.2514/6.2019-0091

[6] Berry, S., “Comparison of BOLT Results from Tests 7026 & 7031 in 20” Mach 6 Tunnel.”

[7] Buck, G., “Surface Temperature/Heat Transfer Measurement Using a Quantitative Phosphor Thermography System,” presented at the 29th Aerospace Sciences Meeting, Reno, NV,U.S.A., 1991. https://doi.org/10.2514/6.1991-64

[8] Berger, K. T., Hollingsworth, K. E., Wright, S. A., and Rufer, S. J., “NASA Langley Aerothermodynamics Laboratory: Hypersonic Testing Capabilities,” presented at the 53rd AIAA Aerospace Sciences Meeting, Kissimmee, Florida, 2015. https://doi.org/10.2514/6.2015-1337

[9] Gnoffo, P. A., and Cheatwood, F. M., “User’s Manual for the Langley Aerothermodynamic Upwind Relaxation Algorithm (LAURA),” NAS 1.15:4674, April 1996.

[10] Rieken, E., Berry, S. A., Broslawski, C., and Greene, F. A., “Aeroheating Measurements of BOLT Aerodynamic Fairings and Transition Module,” presented at the AIAA Scitech 2020 Forum, Orlando, FL, 2020. https://doi.org/10.2514/6.2020-1561

[11] Wolfe, William L. and Georges Zissis. ‘The Infrared Handbook, Revised Edition.’ (1985).”

[12] Minkina, W., and Dudzik, S., “Infrared Thermography: Errors and Uncertainties,” p. 222.

[13] Cerasuolo, S., “Heat flux measurements by infrared thermography in the Boeing / AFOSR mach-6 Quiet Tunnel,” 2016.

[14] “NIST TN 1297: 2. Classification of Components of Uncertainty,” NIST, 2015. Retrieved 15 May 2024. https://www.nist.gov/pml/nist-technical-note-1297/nist-tn-1297-2-classification-components-uncertainty

[15] Mason, M. L. and Rufer, S. J., "Features of the Upgraded Imaging for Hypersonic Experimental Aeroheating Testing (IHEAT) Software," AIAA 2016-4322, Jun. 2016. doi:10.2514/6.2016-4322.

[16] Merski, N., "Reduction and Analysis of Phosphor Thermography Data with the IHEAT Software Package," presented at the 36th AIAA Aerospace Sciences Meeting and Exhibit, Reno,NV,U.S.A., 1998. https://doi.org/10.2514/6.1998-712

[17] Wernz, S., "Flat-BOLT Surrogates for Investigating Second-Mode and Crossflow Instabilities," AIAA Aviation 2023 Forum, San Diego, California, 2023. doi:10.2514/6.2023-3442.

[18] Hill, J.L., Borg, M.P., Tufts, M.W., Benitez, E.K., and Reeder, M.F., "Leading-Edge Curvature Influence on Hypersonic Boundary Layer Transition," AIAA Scitech 2023 Forum, National Harbor, Maryland, 2023. doi:10.2514/6.2023-0098.

[19] Bemis, B.I., Brun, J.L., Wanstall, C.T., Hill, J.L., Borg, M.P., Redmond, J.L., Ruggeri, M., Jantze, K., Scalo, C., and Running, C.L., "Ultrasonically Absorptive Silicon-Carbide Foam for Boundary-Layer Control," AIAA Scitech 2023 Forum, National Harbor, Maryland, 2023. doi:10.2514/6.2023-0096.

[20] Wernz, S., Basore, K., Scott, C.J., Turbeville, D., and Berry, S., "Experiments on Flat-BOLT Surrogates for Investigating the Impact of the Nose Region on Acreage Heating and Transition to Turbulence," Abstract submitted to the AIAA Scitech 2025 Forum, Orlando, Florida, 2025.